Functionalised hexagonal-domain graphene for position-sensitive photodetectors

Adolfo De Sanctis[1], **Matthew D. Barnes**[1], **Iddo Amit**[1], **Monica F. Craciun**[1] **and Saverio Russo**[1]‡

[1] Centre for Graphene Science, College of Engineering, Mathematics and Physical Sciences, University of Exeter, Exeter EX4 4QF, United Kingdom

E-mail: `s.russo@exeter.ac.uk`

Abstract. Graphene's unique photoresponse has been largely used in a multitude of optoelectronics applications ranging from broadband photodetectors to wave-guide modulators. In this work we extend the range of applications to position-sensitive photodetectors (PSDs) using $FeCl_3$-intercalated hexagonal domains of graphene grown by atmospheric pressure chemical vapour deposition (APCVD). The $FeCl_3$-based chemical functionalisation of APCVD graphene crystals is affected by the presence of wrinkles and results in a non-uniform doping of the graphene layers. This doping profile creates multiple p-p^+ photoactive junctions which show a linear and bipolar photoresponse with respect to the position of a focussed light spot, which is ideal for the realization of a PSD. Our study paves the way towards the fabrication of flexible and transparent PSDs that could be embedded in smart textile and wearable electronics.

PACS numbers: 72.40.+w, 78.67.Wj, 78.30.-j, 61.48.Gh, 68.65.Pq

Keywords: APCVD, graphene, intercalation, photodetector, Raman, position-sensitive.
Submitted to: *Nanotechnology*

---

‡ To whom the correspondence should be addressed

1. Introduction

The isolation of a single layer of graphene [1] has triggered an immense response in the scientific community in the past decade [2, 3]. Both the exceptional electrical and optical properties of this material have been studied in detail and exploited in many areas of pure and applied research. In particular, its broadband absorption and field effect tunability make graphene an excellent platform for optoelectronic devices[4]. The breadth of such devices includes high-responsivity [5] and high-speed [6] broadband photodetectors (PDs), wave-guide coupling [7] and transparent and flexible electrodes [8]. The photoresponse of graphene PDs has been investigated with many techniques, though so far no reports have been made of its application in position sensitive detectors (PSDs). Such devices traditionally consist of a semiconductor (Si or Ge) junction with four contacts, which exploits the *lateral photoeffect* [9], that is the photovoltage generated at the junction plane in the presence of localized illumination, in addition to the conventional photovoltage effect that is formed across the junction. This effect has been extensively studied in the past [10, 11] and it is at the base of PSDs used currently in many applications, such as: laser alignment, motion control, automation and scanning probe microscopy. The detection of focussed X-rays *via* field-effect in a graphene transistor has been shown [12] though no other uses of graphene for PSDs in the UV-visible-NIR spectral range have been reported.

In this work we present the first chemical functionalisation of multilayer hexagonal domains of graphene grown by atmospheric pressure chemical vapour deposition (APCVD) [13] and demonstrate its use as an all-graphene PSD. Pristine graphene presents fundamental limitations in optoelectronic applications, such as an low intrinsic conductivity and the lack of bandgap. Chemical functionalisation [14] has been employed in the past years to overcome such limitations providing researchers with a stable and robust platform, thanks to the opening of an energy bandgap [15] or an increase in the conductivity of graphene. Amongst the different forms of functionalisation, intercalation with $FeCl_3$ [16], is used to induce strong p-type doping in the graphene layers, making it particularly suitable for use as transparent electrodes [17, 18]. It has been recently reported that can $FeCl_3$-intercalated graphene, employed in a light emitting device, gives an enhanced light emission of 60% compared to standard graphene electrodes and up to 40% enhancement compared to commercial conductive polymers [8] while having an unprecedented stability in ambient conditions [19]. Here we intercalate multilayer (2-3 layers) hexagonal crystals of graphene with $FeCl_3$ and characterize them using Raman spectroscopy and AFM microscopy. After intercalation, we fabricate a multi-terminal device and characterize it using scanning photocurrent mapping microscopy (SPCM) [20]. The formation of wrinkles in the as-grown graphene is associated with the observed photoresponse of the device, in agreement with the charge density distribution measured across the device, using Raman spectroscopy mapping. Several junctions between regions of high (p^+) and low (p) doping are observed and the position of such p-p^+ junctions correlates well with the observed photocurrent.

Furthermore, the photoresponse scales linearly with the position of the excitation source and changes sign at the centre of the p-p$^+$ junctions. The observed linearity and bipolarity make our device suitable for position-sensitive detection of focused light. Our findings, combined with the high stability of $FeCl_3$-intercalated graphene [19] and the ability to grow millimetre-sized single crystals [13], fill a technological gap in the inventory of all-graphene devices and open a route towards the fabrication of flexible PSDs for a multitude of novel applications.

2. Experimental methods

2.1. Graphene growth and intercalation

Multilayer hexagonal domains of graphene were grown on copper by APCVD [21] using a melting/re-solidification pre-treatment step to reduce nucleation density and increase domain size. Growth was carried out at $\sim 1075°C$ using diluted CH_4 (1000 ppm) as the carbon precursor and a high H_2/CH_4 (50/25 sccm) to aid multilayer formation. The crystals where then transferred to highly doped Si substrate capped with 285 nm thermal SiO_2 using PMMA-supported electrochemical delamination [22, 23]. The delamination step was performed using a 0.5 M NaCl solution and glassy carbon anode at 0.5 A, followed by rinsing in de-ionised water.

The intercalation with $FeCl_3$ was performed using a previously reported vapour phase method in vacuum [16]. More specifically, graphene on SiO_2/Si and anhydrous $FeCl_3$ (Sigma-Aldrich, powder, $\geq 99.99\,\%$ trace metals basis) are placed in a glass tube of a multi-zone resistive heated furnace. The glass tube is sealed after evacuating it to a pressure $< 10^{-5}$. Hence the sample is heated at a temperature of 360 °C and the $FeCl_3$ at the sublimation temperature of 315 °C for 12 hours. The furnace is then left to cool and the sample removed.

After the intercalation, samples were washed in Acetone and Isopropyl alcohol (IPA) in order to remove $FeCl_3$ residues from the substrate. The quality of the growth, the transfer and the degree of intercalation with $FeCl_3$ was assessed via optical inspection, atomic force microscopy (AFM) and micro-Raman spectroscopy. All measurements were performed in atmosphere and at room temperature. Raman spectra were acquired using a *Renishaw* spectrometer, with 532 nm excitation laser with incident power density of $0.3 - 1$ MW/cm^2 through a ×50 objective lens. The scattered light was dispersed by a 2400 g/mm grating and recorded by a CCD with 5 seconds integration time. Raman maps were acquired with the same setup performing a raster scan of the area in 0.5 μm steps. AFM topography and phase image were acquired with a *Bruker Innova* AFM system, operating in the "tapping" mode using a sharp (radius of curvature $<$ 10 nm) highly doped silicon tip from "Nanosensors" with a nominal resonance frequency of 330 kHz.

2.2. Devices fabrication and characterization

Multi-terminal photodetectors were fabricated on the same substrates. Metal contacts were defined via electron-beam lithography using 300 nm thick PMMA as resist, followed by electron-beam evaporation of Ti/Au (5/50 nm) and lift-off in acetone. The sample was then contacted to the chip carrier by mean of wedge bonding using 20 μm thick gold wire. Scanning photocurrent microscopy (SPCM) was performed using a custom-built setup [20]: a laser beam ($\lambda_{\text{in}} = 375\,\text{nm}$) was focussed on the sample by a ×50 objective lens to a $\sim$ 260 nm spot diameter. The sample was mounted on a motorized microscope stage and raster-scanned under the laser beam. The photoresponse of the device was measured in short-circuit configuration for each point, producing a two-dimensional map of the photogenerated current (see also figure 3a). The light of the laser was modulated at a frequency of 33.25 Hz and the current measured via an *Ametek* 7270 DSP Lock-in amplifier locked at the same frequency.

3. Results and discussion

3.1. Functionalization of graphene single crystals

Figure 1a shows the optical micrographs and Raman spectra of a pristine, as-transferred, multi-layer hexagonal domain of graphene grown by APCVD. Each layer grows in a stacked sequence, where the multi-layers appear at the centre of the first single-layer indicating that they share the same nucleation site [24]. The Raman spectrum of the first layer (1) shows the two main features of graphene: the G peak at $\sim 1585\,\text{cm}^{-1}$, originating from the resonant $E_{2\text{g}}$ mode and the 2D peak at $\sim 2700\,\text{cm}^{-1}$, originating from the double-resonant $A_{1\text{g}}$ mode [25]. The shape of the 2D band, a single Lorentzian peak, and intensity ratio $I_{2\text{D}}/I_{\text{G}} \sim 1.9$ confirm the single-layer nature of the graphene. The spectrum of the second layer (2) shows the same features but with a ratio $I_{2\text{D}}/I_{\text{G}} \sim 3.36$, which deviates from the expected ratio for two AB-stacked graphene layers [26]. This is due to the rotation of the crystallographic axes with respect to the underlying layer, producing an effective decoupling of the two stacked layers [27, 21]. The third layer (3) is slightly twisted with respect to the second, as shown by optical inspection, and the spectrum shows a 2D band that can be fitted with the convolution of 4 Lorentzian peaks, which is characteristic of twisted bilayer graphene with a twist angle $< 3°$ [21, 28]. These observations are common to all the crystals we examined.

Functionalization with $FeCl_3$ strongly affects the electronic characteristics of graphene [14, 17]. $FeCl_3$ intercalates between the layers of graphene forming a stacked sequence of graphene/intercalant/graphene [29]. Charge transfer to the $FeCl_3$ layer causes p-doping of the graphene [16], which results in the non-adiabatic removal of the Kohn anomaly at the Γ point and the consequent stiffening of the $E_{2\text{g}}$ mode of graphene [30]. This stiffening is observed in the upshift of the G peak [31, 32, 33] in the Raman spectrum of graphene. Figure 1b presents the optical micrograph and the Raman spectra of the intercalated flake. Optically we can see each hexagonal crystal, with a change in contrast due to the presence of $FeCl_3$. The Raman spectra are acquired in the same locations as in figure 1a. The first layer (1) shows an upshift of the position of the G peak to $1600\,cm^{-1}$ and an increase in the height ($I_{2D}/I_G \sim 0.92$), both indicating small doping of the graphene [33]. The second (2) and third (3) layers show the same characteristic spectra. We observe a split of the G band into three peaks, each corresponding to different doping levels: the G_0-peak is the signature of pristine graphene; the G_1-peak is given by a graphene layer in contact with one $FeCl_3$ layer (stage-2) and the G_2-peak is given by one layer of graphene sandwiched between two $FeCl_3$ layers (stage-1). The 2D-band is also indicative of the effective decoupling of the graphene layers by the intercalant, as can be seen in the third spectrum, the multi-peak structure is reduced to a single Lorentzian peak, signature of the loss of stacking order within the graphene layers. The peaks related to the $FeCl_3$ molecules lie at significant lower energies ($100 - 400$ cm^{-1}) [34], therefore they do not interfere with the modes of graphene. These results confirm the successful intercalation of single crystal APCVD graphene with $FeCl_3$.

To evaluate the quality of our intercalated APCVD graphene we used AFM. Figure 2a-b show the topography image of a pristine single crystal, with a second layer grown at the centre, as seen optically (inset). Here we observe a series of parallel wrinkles (green arrows), which match the topography of the re-solidified copper used as metal catalyst during the growth. More interestingly, we observe larger wrinkles running in the perpendicular direction with respect to the first ones, originating from the centre of the crystal (blue arrows) and ending close to the middle of the hexagon's side. Wrinkles in APCVD graphene have been previously reported [23, 35] to form during the cooling stage due to the different thermal expansion coefficients of graphene and copper. In the same images, residues of PMMA from the transfer process appear as white dots, as previously reported [36].

Intercalation with $FeCl_3$ changes the topography of the single crystals. Figure 2c-d show the AFM topography and phase images of an intercalated single crystal. In this case the image was acquired after fabrication of metal contacts. Focusing on the topographic features we immediately notice the absence of the substrate-related wrinkles, while a number of bubble-like structures are still present and the cross-directional wrinkles can still be seen (blue arrows). The disappearance of small wrinkles is attributed to the intercalation process: by separating the graphene layers, the intercalant allows them to relax. The AFM phase image can readily distinguish between different materials, as it represents the phase lag between the tip excitation signal and its motion that is due to the (viscoelastic) damping properties of the sample [37]. In figure 2d it can be seen that the bubble-like structures observed in topography show a clear phase contrast. Since no annealing was performed after the transfer of graphene form the copper substrate, the PMMA residues observed before intercalation are still present during the process. The distribution and density is, indeed, comparable with what is observed in the pristine crystal, suggesting that those structures are caused by the contamination of graphene, arising from the transfer process. Clustering of $FeCl_3$

around these areas can contribute to the observed contrast. The presence of wrinkles, in particular along the crossed lines which extends from the centre of the crystal to the sides of the hexagon, is still clearly visible.

3.2. APCVD graphene photodetectors

Having successfully intercalated single crystal multi-layer graphene, we proceed to study its optoelectronic properties. Figure 3a shows a schematic representation of a multi-terminal device. Here the contacts have been positioned in parallel to the sides of the top-layer hexagon, as shown in the optical micrograph (figure 3b). The resistance across two opposing pair of contacts, namely 1-4 and 3-6 in figure 3a-b, was $R_{1-4} = 660 \pm 2\,\Omega$ and $R_{3-6} = 670 \pm 2\,\Omega$, in agreement with previous measurements [16]. The photoresponse of the device was characterized using SPCM, employing different pairs of contacts. Figure 3c-d show the SPCM maps acquired with two different pairs of contacts (1-4 and 3-6, respectively). Both SPCM maps show photocurrent I_{ph} being generated across the whole device, with a net change in sign appearing at the centre of it, in the direction orthogonal to the contacts. The dashed black lines in panels c and d mark the position of the maxima of the photocurrent. Measuring across both pair of contacts and summing the two signals we obtain a SPCM map which displays a clear four-fold symmetry of the photocurrent (PC), as shown in figure 3e where the black dashed lines are the same as in panels c and d. Superimposing these lines, extrapolated from the SPCM map, onto the AFM maps of the same device, shown in figure 2c-d, we see that they match with the observed crossed wrinkles in the graphene crystal.

The role of grain boundaries and wrinkles in graphene-based photodetectors has been studied via near-field photocurrent nanoscopy, where the presence of grain boundaries was associated with a reversal in the sign of the photocurrent while enhanced PC was observed in the presence of wrinkles [38]. The growth of hexagonal domains by APCVD is known to give high-quality, defect-free, graphene. Therefore, we do not expect any grain boundaries to be present across the device. All our observations point towards the fact that the observed PC is related to the intercalation spatial inhomogeneity, and thus to the doping inhomogeneity, of the graphene crystals. The presence of wrinkles is likely to create clusters of $FeCl_3$, increasing the level of doping in those regions, while sign reversal is related to a sharp change in doping, forming a p-p$^+$ junction in the highly doped graphene. These junctions can therefore act as photoactive centres giving the observed photoresponse for the overall device.

To confirm these hypotheses we acquired a Raman map of the device (see methods). In figure 4a-d we report the fit of Lorentzian peaks to the G-band region, as previously discussed (see figure 1b). Figure 4a-b show the height and position of the G_0 peak, respectively, while the G_1 band is shown in figure 4c-d. The presence of a blueshifted G_0 peak which agrees very well the boundaries of the crystal and indicates areas with partial intercalation of $FeCl_3$ within the graphene layers. We observe that the G_1 peak height decreases significantly across a sign reversal in photocurrent (the cross-shaped structure). This decrease in height is also accompanied by a redshift of the G_1 peak, from $\sim 1612\,\text{cm}^{-1}$ to $\sim 1605\,\text{cm}^{-1}$, in the same region, as shown in figure 4d. Using the model developed by Lazzeri *et al.* [30] to extrapolate the total density of holes in doped graphene from the position of the G-band peaks. It has been shown that this model gives an estimation of the charge density within 10% of the values extrapolated with transport techniques [17]. The results are shown in figure 4e: here we see that a gradient of charge density is present along the two lines determined by the photocurrent maps, confirming our hypotheses.

The PMMA residues observed in figure 2a-d, do not contribute to the observed doping, and therefore to the photoresponse, since the charge transfer due to residual PMMA ($\sim 10^{11}$ cm^{-2}, see [36]) is negligible compared to the high level of doping induced by the intercalation with FeCl_3 ($> 4 \cdot 10^{13}$ cm^{-2}).

3.3. Towards graphene-based position-sensitive photodetectors

The unique photocurrent distribution, with a four-fold symmetry, observed in our device (figure 3e), can be used for position-sensitive applications. Commercial position-sensitive photodetectors (PSDs) exploit the photovoltage generated parallel to a semiconductor junction in the presence of local illumination [9]. This effect has been extensively studied in the past [10, 11] and is characterized by a bipolar linear photoresponse as function of illumination position. Figures 5a-c show the line profiles extrapolated from the SPCM maps in figure 3c-d, while figures 5b-d show the same line profiles acquired on the charge density n_h maps in figure 4e. The mean value of the log-normal distribution of n_h ($\overline{n_h} = (4.27 \pm 0.02) \cdot 10^{13}\,\text{cm}^{-2}$) separates values $n_h < \overline{n_h}$ (low doping, p regions) and $n_h > \overline{n_h}$ (high doping, p$^+$ regions). We can clearly see that the extremes of I_{ph} are located where n_h crosses $\overline{n_h}$, i.e. in the presence of a p-p$^+$ junction. At the same time, bipolar linear regions are present (green lines), where the photocurrent changes sign at the centre of the photoactive junction. This behaviour is very similar to what is observed in a *lateral* photoactive junction [9]. In this case the junction is formed between areas of different doping in the functionalised graphene, induced by the inhomogeneity of the FeCl_3 intercalation driven by the wrinkles in the pristine APCVD single crystals. Therefore, exploiting a multi-terminal geometry as the one adopted here, it is possible to use these linear regions to determine the position of a focussed light spot on the device.

4. Conclusion

In conclusion, we have shown that multilayer APCVD-grown hexagonal crystals of graphene can be intercalated with FeCl_3 and used as position-sensitive photodetectors. We characterized the degree of intercalation and the resulting doping of graphene, showing the formation of multiple p-p$^+$ junctions associated with the presence of wrinkles in the pristine APCVD crystals. We then characterized the photoresponse of a multi-terminal device showing a strong spatial correlation between the observed photocurrent and the p-p$^+$ junctions. The photoresponse is found to be a linear function of the laser spot position and changes sign at the centre of each junction. This behaviour, combined with a four-fold pattern in the spatially resolved photocurrent, make these devices ideal candidates for position sensitive detection of focussed light. Furthermore, all measurements have been repeated after $\sim$ 11 months exposure of the device to environmental conditions, showing no change in the photoresponse, in agreement with the previously reported stability of this material [19]. These findings pave the way to additional functionality in graphene-based optoelectronic devices and open a new route towards flexible, lightweight, transparent and highly stable PSDs, with possible employment in smart textile and wearable electronics [39].

Acknowledgements

S. Russo and M.F. Craciun acknowledge financial support from EPSRC (Grant no. EP/J000396/1, EP/K017160/1, EP/K010050/1, EPG036101/1, EP/M001024/1, EPM002438/1), from Royal Society international Exchanges Scheme 2016/R1, from European Commission (FP7-ICT-2013-613024-GRASP) and from The Leverhulme trust (grant title ”Quantum Drums” and ”Room temperature quantum electronics”). I. Amit received funding from the People Programme (Marie Curie Actions) of the European Union’s Eighth Framework Programme Horizon 2020 under REA grant agreement number 701704.

Author contributions

A.De.S. and M.D.B. conceived the experiment. A.De.S. conducted the intercalation of the graphene, fabricated and measured the devices, analysed the data and wrote the manuscript. M.D.B. grew and transferred the APCVD graphene. I. A. performed the AFM measurements. M.F.C. and S.R. supervised the project. All authors contributed to the interpretation of the results and editing of the manuscript.

Additional information

Correspondence should be addressed to S.R.

Competing financial interest

The authors declare no competing financial interest.

References

[1] K. S. Novoselov, A. K. Geim, S. V. Morozov, D. Jiang, Y. Zhang, S. V. Dubonos, I. V. Grigorieva, and A. A. Firsov. Electric field effect in atomically thin carbon films. *Science*, 306(5696):666–669, 2004.

[2] A. K. Geim and K. S. Novoselov. The rise of graphene. *Nat Mater*, 6(3):183–191, Mar 2007.

[3] A. K. Geim. Graphene: Status and prospects. *Science*, 324(5934):1530–1534, 2009.

[4] F. H. L. Koppens, T. Mueller, Ph Avouris, A. C. Ferrari, M. S. Vitiello, and M. Polini. Photodetectors based on graphene, other two-dimensional materials and hybrid systems. *Nat Nano*, 9(10):780–793, Oct 2014.

[5] Chang-Hua Liu, You-Chia Chang, Theodore B. Norris, and Zhaohui Zhong. Graphene photodetectors with ultra-broadband and high responsivity at room temperature. *Nat Nano*, 9(4):273–278, Apr 2014.

[6] Thomas Mueller, Fengnian Xia, and Phaedon Avouris. Graphene photodetectors for high-speed optical communications. *Nat Photon*, 4(5):297–301, May 2010.

[7] Xiaomu Wang, Zhenzhou Cheng, Ke Xu, Hon Ki Tsang, and Jian-Bin Xu. High-responsivity graphene/silicon-heterostructure waveguide photodetectors. *Nat Photon*, 7(11):888–891, Nov 2013.

[8] Elias Torres Alonso, George Karkera, Gareth F. Jones, Monica F. Craciun, and Saverio Russo. Homogeneously bright, flexible, and foldable lighting devices with functionalized graphene electrodes. *ACS Applied Materials & Interfaces*, 8(26):16541–16545, 2016.

[9] J. Torkel Wallmark. A new semiconductor photocell using lateral photoeffect. *Proc. IRE vol. 45, pp. 474-483, April 1957*, 45:474–483, April 1957.

[10] Gerald Lucovsky. Photoeffects in nonuniformly irradiated p-n junctions. *Journal of Applied Physics*, 31(6):1088–1095, 1960.

[11] T. G. Carr, J. C. Richmond, and R. G. Wagner. Position-sensitive schottky barrier photodiodes: Time-dependent signals and background saturation effects. *IEEE Transactions on Electron Devices*, 17(7):507–513, Jul 1970.

[12] Edward Cazalas, Biddut K. Sarker, Michael E. Moore, Isaac Childres, Yong P. Chen, and Igor Jovanovic. Position sensitivity of graphene field effect transistors to X-rays. *Applied Physics Letters*, 106(22), 2015.

[13] Ali Mohsin, Lei Liu, Peizhi Liu, Wan Deng, Ilia N. Ivanov, Guoliang Li, Ondrej E. Dyck, Gerd Duscher, John R. Dunlap, Kai Xiao, and Gong Gu. Synthesis of millimeter-size hexagon-shaped graphene single crystals on resolidified copper. *ACS Nano*, 7(10):8924–8931, 2013.

[14] M F Craciun, I Khrapach, M D Barnes, and S Russo. Properties and applications of chemically functionalized graphene. *Journal of Physics: Condensed Matter*, 25(42):423201, 2013.

[15] Steven E. Martins, Freddie Withers, Marc Dubois, Monica F. Craciun, and Saverio Russo. Tuning the transport gap of functionalized graphene via electron beam irradiation. *New Journal of Physics*, 15(3):033024, 2013.

[16] Ivan Khrapach, Freddie Withers, Thomas H. Bointon, Dmitry K. Polyushkin, William L. Barnes, Saverio Russo, and Monica F. Craciun. Novel highly conductive and transparent graphene-based conductors. *Advanced Materials*, 24(21):2844–2849, 2012.

[17] Thomas H. Bointon, Gareth F. Jones, Adolfo De Sanctis, Ruth Hill-Pearce, Monica F. Craciun, and Saverio Russo. Large-area functionalized CVD graphene for work function matched transparent electrodes. *Scientific Reports*, 5:16464, Nov 2015.

[18] Thomas H. Bointon, Monica F. Craciun, and Saverio Russo. Is graphene a good transparent electrode for photovoltaics and display applications? *IET Circuits, Devices and Systems*, 9:403–412(9), November 2015.

[19] Dominique J. Wehenkel, Thomas H. Bointon, Tim Booth, Peter Boggild, Monica F. Craciun, and Saverio Russo. Unforeseen high temperature and humidity stability of $FeCl_3$ intercalated few layer graphene. *Scientific Reports*, 5:7609, Jan 2015.

[20] Adolfo De Sanctis, Gareth F. Jones, Nicola J. Townsend, Monica F. Craciun, and Saverio Russo. An integrated and multi-purpose microscope for the characterization of atomically thin optoelectronic devices. *arXiv:1609.07514*, 2016.

[21] Rui He, Ting-Fung Chung, Conor Delaney, Courtney Keiser, Luis A. Jauregui, Paul M. Shand, C. C. Chancey, Yanan Wang, Jiming Bao, and Yong P. Chen. Observation of low energy Raman modes in twisted bilayer graphene. *Nano Letters*, 13(8):3594–3601, 2013.

[22] Yu Wang, Yi Zheng, Xiangfan Xu, Emilie Dubuisson, Qiaoliang Bao, Jiong Lu, and Kian Ping Loh. Electrochemical delamination of CVD-grown graphene film: Toward the recyclable use of copper catalyst. *ACS Nano*, 5(12):9927–9933, 2011. PMID: 22034835.

[23] Libo Gao, Wencai Ren, Huilong Xu, Li Jin, Zhenxing Wang, Teng Ma, Lai-Peng Ma, Zhiyong Zhang, Qiang Fu, Lian-Mao Peng, Xinhe Bao, and Hui-Ming Cheng. Repeated growth and bubbling transfer of graphene with millimetre-size single-crystal grains using platinum. *Nat Commun*, 3:699, Feb 2012.

[24] Ali Mohsin, Lei Liu, Peizhi Liu, Wan Deng, Ilia N. Ivanov, Guoliang Li, Ondrej E. Dyck, Gerd Duscher, John R. Dunlap, Kai Xiao, and Gong Gu. Synthesis of millimeter-size hexagon-shaped graphene single crystals on resolidified copper. *ACS Nano*, 7(10):8924–8931, 2013.

[25] Andrea C. Ferrari and Denis M. Basko. Raman spectroscopy as a versatile tool for studying the properties of graphene. *Nat Nano*, 8(4):235–246, Apr 2013.

[26] L.M. Malard, M.A. Pimenta, G. Dresselhaus, and M.S. Dresselhaus. Raman spectroscopy in graphene. *Physics Reports*, 473(56):51 – 87, 2009.

[27] Daniel R. Lenski and Michael S. Fuhrer. Raman and optical characterization of multilayer turbostratic graphene grown via chemical vapor deposition. *Journal of Applied Physics*, 110(1), 2011.

[28] Y. Cao, J. Y. Luo, V. Fatemi, S. Fang, J. D. Sanchez-Yamagishi, K. Watanabe, T. Taniguchi, E. Kaxiras, and P. Jarillo-Herrero. Superlattice-induced insulating states and valley-protected orbits in twisted bilayer graphene. *Phys. Rev. Lett.*, 117:116804, Sep 2016.

[29] J.M. Thomas, G.R. Millward, R.F. Schlogl, and H.P. Boehm. Direct imaging of a graphite intercalate: Evidence of interpenetration of “stages” in graphite: Ferric chloride. *Materials Research Bulletin*, 15(5):671 – 676, 1980.

[30] Michele Lazzeri and Francesco Mauri. Nonadiabatic Kohn anomaly in a doped graphene monolayer. *Phys. Rev. Lett.*, 97:266407, Dec 2006.

[31] Weijie Zhao, Ping Heng Tan, Jian Liu, and Andrea C. Ferrari. Intercalation of few-layer graphite flakes with $FeCl_3$: Raman determination of fermi level, layer by layer decoupling, and stability. *Journal of the American Chemical Society*, 133(15):5941–5946, 2011. PMID: 21434632.

[32] Da Zhan, Li Sun, Zhen Hua Ni, Lei Liu, Xiao Feng Fan, Yingying Wang, Ting Yu, Yeng Ming Lam, Wei Huang, and Ze Xiang Shen. $FeCl_3$-based few-layer graphene intercalation compounds: Single linear dispersion electronic band structure and strong charge transfer doping. *Advanced Functional Materials*, 20(20):3504–3509, 2010.

[33] Das A., Pisana S., Chakraborty B., Piscanec S., Saha S K., Waghmare U V., Novoselov K S., Krishnamurthy H R., Geim A K., Ferrari A C., and Sood A K. Monitoring dopants by raman scattering in an electrochemically top-gated graphene transistor. *Nat Nano*, 3(4):210–215, Apr 2008.

[34] N. Caswell and S.A. Solin. Vibrational excitations of pure $FeCl_3$ and graphite intercalated with ferric chloride. *Solid State Communications*, 27(10):961 – 967, 1978.

[35] Yimin A. Wu, Ye Fan, Susannah Speller, Graham L. Creeth, Jerzy T. Sadowski, Kuang He, Alex W. Robertson, Christopher S. Allen, and Jamie H. Warner. Large single crystals of graphene on melted copper using chemical vapor deposition. *ACS Nano*, 6(6):5010–5017, 2012.

[36] A. Pirkle, J. Chan, A. Venugopal, D. Hinojos, C. W. Magnuson, S. McDonnell, L. Colombo, E. M. Vogel, R. S. Ruoff, and R. M. Wallace. The effect of chemical residues on the physical and electrical properties of chemical vapor deposited graphene transferred to SiO_2. *Applied Physics Letters*, 99(12), 2011.

[37] Ricardo García and Ruben Perez. Dynamic atomic force microscopy methods. *Surface science reports*, 47(6):197–301, 2002.

[38] Achim Woessner, Pablo Alonso-Gonzalez, Mark B. Lundeberg, Yuanda Gao, Jose E. Barrios-Vargas, Gabriele Navickaite, Qiong Ma, Davide Janner, Kenji Watanabe, Aron W. Cummings, Takashi Taniguchi, Valerio Pruneri, Stephan Roche, Pablo Jarillo-Herrero, James Hone, Rainer Hillenbrand, and Frank H. L. Koppens. Near-field photocurrent nanoscopy on bare and encapsulated graphene. *Nat Commun*, 7, Feb 2016.

[39] A. I. S. Neves, T. H. Bointon, L. V. Melo, S. Russo, I. de Schrijver, M. F. Craciun, and H. Alves. Transparent conductive graphene textile fibers. *Scientific Reports*, 5:9866, May 2015.

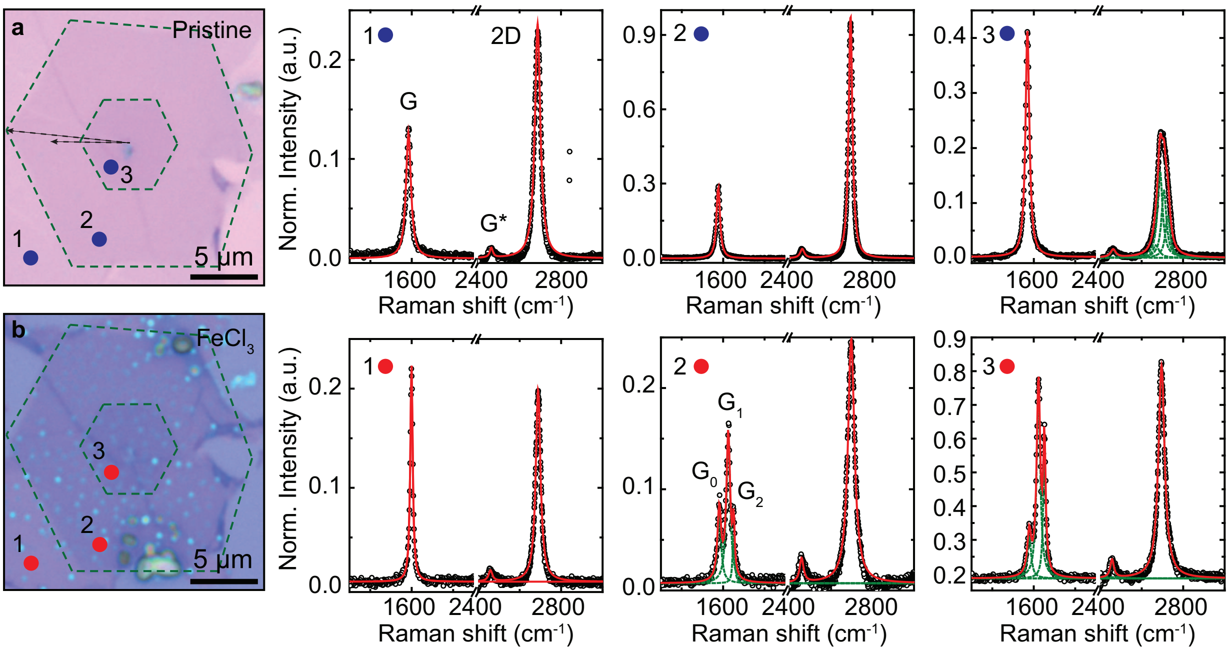

Figure 1. (a) Optical micrograph (left) and Raman spectra (right) of pristine APCVD graphene hexagonal crystals on three different locations: (1) First crystal on substrate, (2) Second layer grown on the first, (3) third layer. Dashed lines indicate the twisting of the hexagonal crystals. (b) Optical micrograph and Raman spectra of the same crystals after intercalation with $FeCl_3$. Raman spectra are normalized to the height of the 1-TO mode of Si at 520 cm^{-1}.

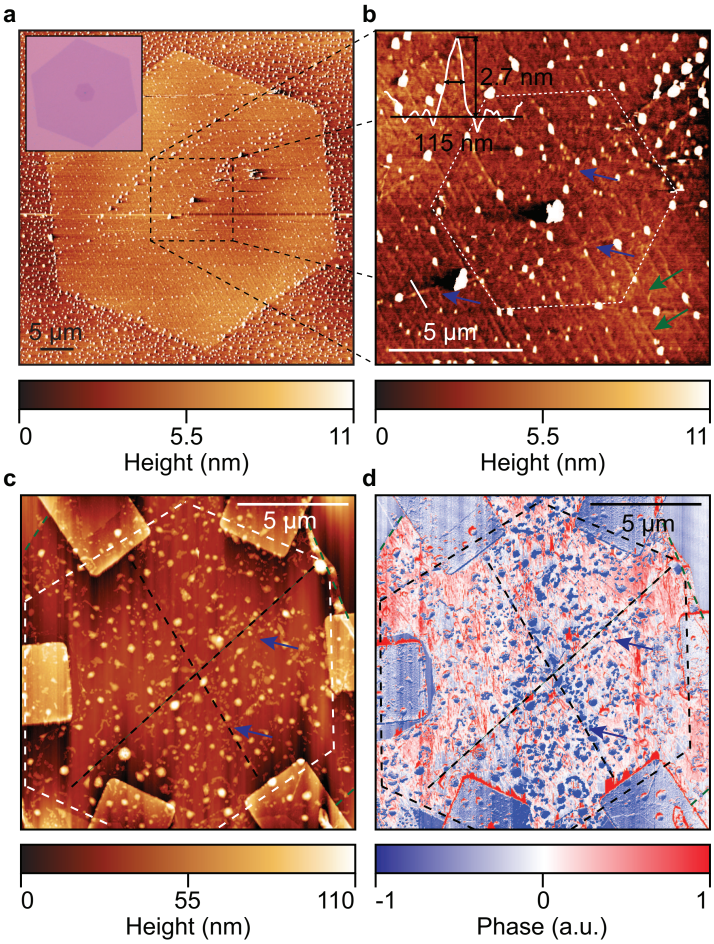

Figure 2. (a) AFM topography of a pristine APCVD graphene hexagonal crystal after transferring onto Si/SiO$_2$ substrate. Inset: optical micrograph of the same crystal. (b) High resolution AFM topography of the central area. Blue and green arrows indicate wrinkles. Inset: profile of a wrinkle, height 2.7 nm and width 115 nm. (c) AFM topography of a graphene hexagonal crystal after intercalation with FeCl$_3$ and fabrication of a multi-terminal photodetector device (see main text). (d) Tapping phase image of the same device. Dashed lines as in figure 3, blue arrows indicate the residual wrinkles. White dots are PMMA residues from the transfer process (see main text).

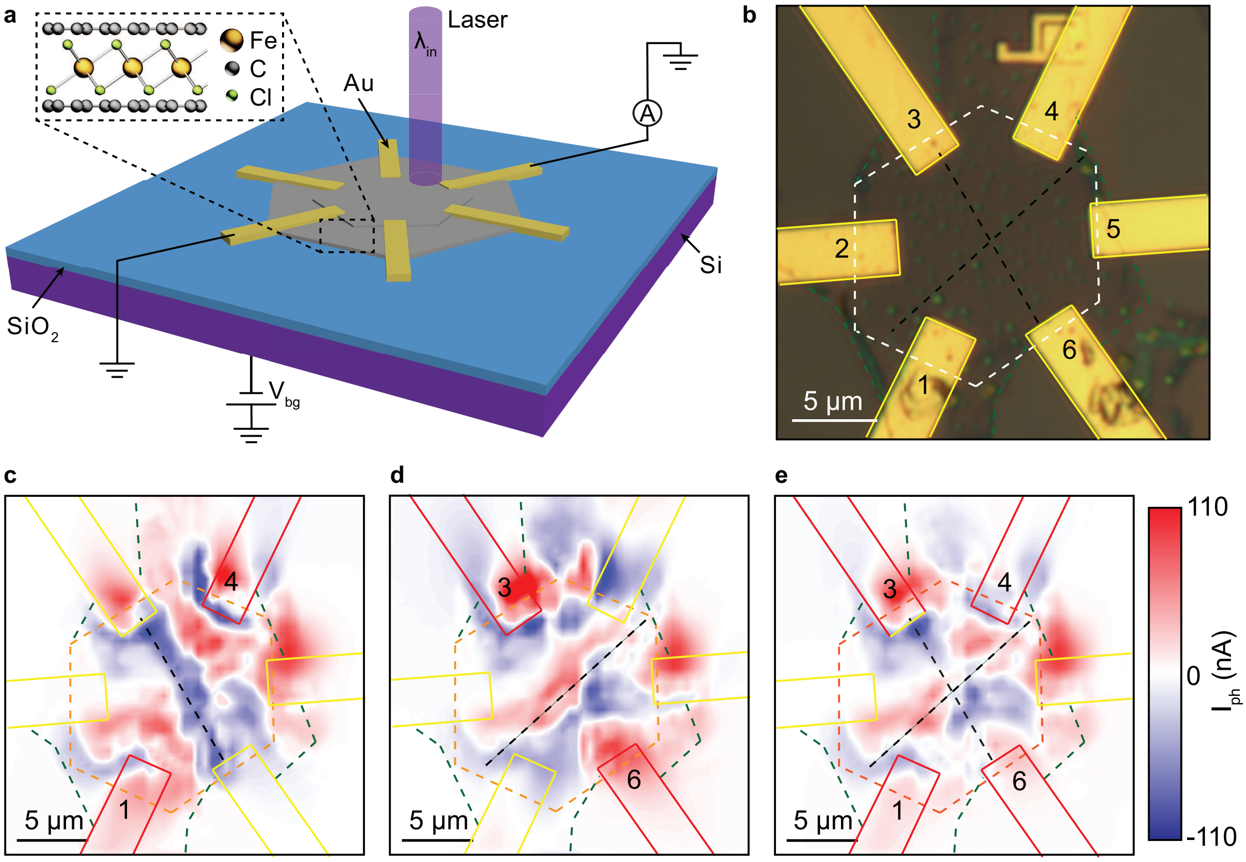

Figure 3. (a) Schematic of the multi-terminal device and measuring geometry. A laser of incident wavelength λ_{in} is scanned across the surface and the electrical response is measured in short-circuit configuration, producing a 2D map of the generated photocurrent. Inset: layer structure of $FeCl_3$-intercalated graphene. (b) Optical micrograph of the device. (c) SPCM map with contacts 3 and 6 connected. (d) SPCM map with terminals 1 and 4. (e) Sum of the SPCM maps shown in panels (c) and (d). Dashed green lines mark the first graphene layer while dashed hexagons (white and orange) mark the second. Dashed black lines indicate the regions in the flake where I_{ph} reverses sign.

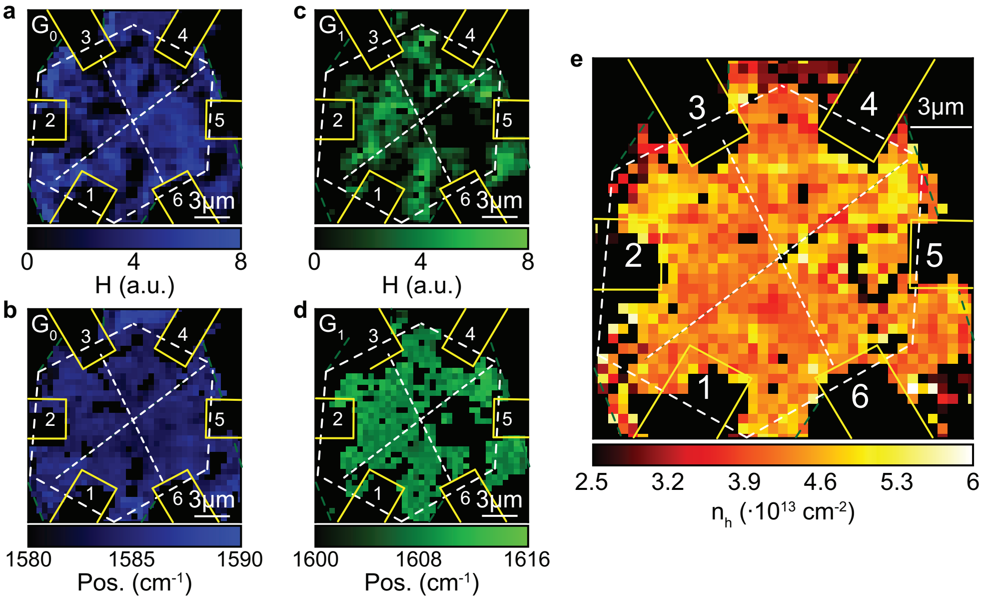

Figure 4. Raman maps of the the multi-terminal device. (a) G_0 peak height. (b) G_0 peak position. (c) G_1 peak height. (d) G_1 peak position. (e) Total intercalation-induced hole concentration in the crystal. Solid and dashed lines as in figure 3.

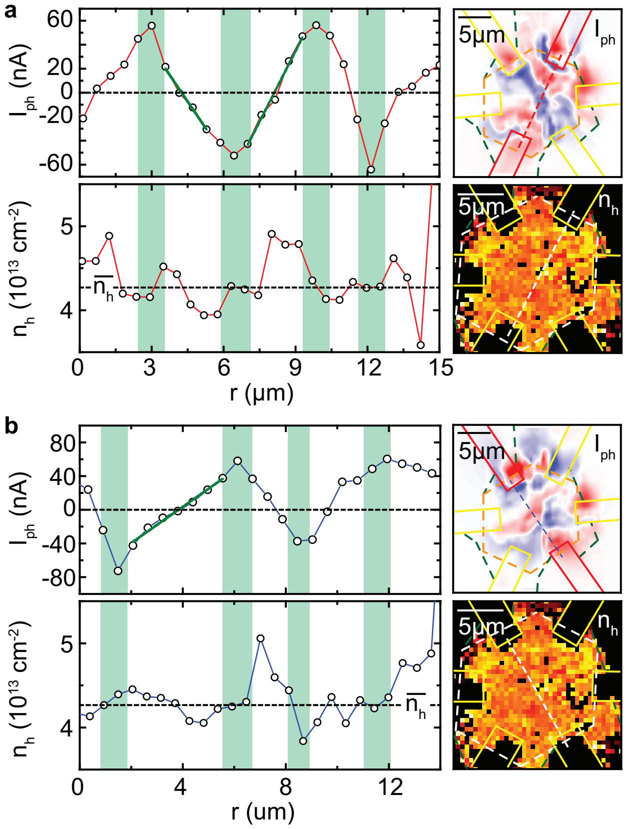

Figure 5. (a) Line profiles of photocurrent I_{ph} (top) and total hole density n_h (bottom) taken along the dashed lines shown in the right panels, with contacts 3 and 6 connected. (b) Same line profiles as in (a) with contacts 1 and 4. Green solid lines mark the linear regions, green-shaded areas mark the maxima and minima of the PC and the corresponding hole density. $\overline{n_h}$ is the log-normal mean value of the reported data.